

Measurement-device agnostic quantum tomography

Robert Stárek,* Martin Bielak, and Miroslav Ježek

Department of Optics, Faculty of Science, Palacký University, 17. listopadu 12, 77146 Olomouc, Czechia

Characterization of quantum states and devices is paramount to quantum science and technology. The characterization consists of individual measurements, which are required to be precisely known. A mismatch between actual and assumed constituent measurements limits the accuracy of this characterization. Here, we show that such a mismatch introduces reconstruction artifacts in quantum state tomography. We use these artifacts to detect and quantify the mismatch and gain information about the actual measurement operators. It consequently allows the mitigation of systematic errors in quantum measurement and state preparation.

I. INTRODUCTION

The measurements play a central role in quantum science and technology [1]. However, the implemented measurements often differ from the ideal ones, leading to systematic errors. One can compensate for these systematic errors with the knowledge of the actual measurements. We investigate this problem from the point of view of quantum tomography, one of the most valuable tools in quantum science [2–6]. It allows the complete characterization of prepared states and implemented quantum circuits, assessing and certifying their quality. Quantum state tomography consists of a suitable set of known measurements on the investigated objects. One can reconstruct the state from the collection of measurement outcomes, the tomogram. Imperfect realization of these measurements causes a mismatch between the assumed and the realized measurement operators. Such a mismatch leads to the wrong interpretation of the acquired tomogram and manifests as a reconstruction artifact.

The true measurement operators can be fully characterized with measurement tomography [7–10], which relies on perfect knowledge of input probe quantum states. Such a requirement is difficult to meet in the experiments. A self-consistent tomography framework has been introduced to loosen this condition [11]. The framework suggests the existence of a self-calibrating state class, which could reveal, when measured, the initially unknown information about the states and the measurement device. Another approach demonstrated for polarization states of light infers a single unknown parameter of the measurement device using maximum likelihood estimation [12]. There are also schemes that use simultaneous likelihood maximization over both states and devices [13] or states and measurements [14]. Finally, assuming the sparsity of the parameter vector and the low rank of the measured density matrix, the dependence on the measurement device can be relaxed [15].

In this work, we show that an ensemble of single-qubit states of equal purity distributed quasi-uniformly on the Bloch sphere forms a class of self-calibrating states. This

class is convenient in experiments where states are naturally prepared with quasi-equal purity, e.g., in photonics and trapped ions. Advantageously, the precise control, characterization, or even sparsity of such self-calibrating probe states is not required. We show a novel approach to simultaneously calibrating quantum measurements and state preparation. To this end, we exploit artifacts in quantum state reconstruction performed on the self-calibrating probe states. In the multi-qubit setting, we can use the method in a fully scalable way to mitigate systematic errors on each local qubit measurement, effectively mitigating errors in the whole system. The method also applies to quantum device tomography thanks to the state-process duality [1, 16, 17], which allows the quantum processes to be treated as states. Our method is not limited to the determination of an initially unknown parameter shared among all measurement operators in the tomographic scheme; it allows the determination of parameters related to each measurement operator individually. The presented scheme provides the characterization of quantum states independently of measurement device imperfections. General concepts are introduced using numerical simulations, and we support our findings with a photonic experiment.

II. MEASUREMENT OPERATOR MISMATCH ARTIFACT

In quantum state tomography, many copies of an initially unknown state, described by density operator $\hat{\rho}$, are subject to a series of measurements described by measurement operators $\hat{\pi}_j$. These measurement operators should be tomographically complete, and their choice influences the performance of the tomography [18–21]. The resulting collection of measurement outcomes forms the tomogram. The tomogram and the measurement operators are then input into an algorithm, which outputs the density operator. Here, we use the maximum-likelihood reconstruction algorithm [13, 22]. If the actual measurement operators $\hat{\pi}_j'$ differ from those put into the reconstruction method, artifacts appear.

Let us demonstrate the behavior in the simplest scenario of pure probe single-qubit states and projective measurements onto the eigenstates of Pauli operators,

* starek@optics.upol.cz

called Pauli tomography. The measurement operator is realized by two rotation angles, corresponding to rotation about the y - and z -axis and subsequent projection onto computational basis state $|0\rangle\langle 0|$. Throughout the article, we use the computational basis $\{|0\rangle, |1\rangle\}$. The following operators describe the constituent measurements

$$\hat{\pi}_j = \hat{R}_z^\dagger(\phi_j)\hat{R}_y^\dagger(\theta_j)|0\rangle\langle 0|\hat{R}_y(\theta_j)\hat{R}_z(\phi_j), \quad (1)$$

where $\hat{R}_j(\alpha) = \exp(i\hat{\sigma}_j\alpha/2)$ is the rotation generated by the Pauli operator. Then, the corresponding detection probability is given by the Born rule,

$$p_j = \text{Tr}[\hat{\rho}\hat{\pi}_j]. \quad (2)$$

The angles θ_j and ϕ_j for Pauli tomography are provided in Table S2 of the Supplemental Material. Assume that due to experimental imperfections, the actual angles are

$$\theta'_j = \theta_j + \delta_j, \quad (3)$$

$$\phi'_j = \phi_j + \epsilon_j, \quad (4)$$

i.e., we introduce systematic additive errors for each measurement operator. The error vector $\vec{\delta} = \{\delta_j, \epsilon_j\}$ parameterizes the measurement operators $\hat{\pi}'_j = \hat{\pi}_j(\vec{\delta})$. We numerically simulate tomograms using these true measurement operators for many pure probe states covering the Bloch sphere quasi-uniformly. Then, we recon-

struct them assuming the original unperturbed measurement operators $\{\hat{\pi}_j\}$. This mismatch causes the state-dependent purity modulation, shown in Figure 1(a-c). This example shows the apparent purity modulation for the case of an error vector $\vec{\delta}$, whose elements are drawn from a normal distribution with $\sigma = 5$ deg. We quantify the purity modulation in the ensemble of reconstructed states as

$$\Delta P = \max P - \min P, \quad (5)$$

where $P = \text{Tr}(\hat{\rho}^2)$ is the purity of the reconstructed state.

To show how purity modulation scales with the error vector magnitude, we scale it with a non-negative real factor λ , i.e. $\vec{\delta} \rightarrow \lambda\vec{\delta}$, and observe the ΔP , as shown in Figure 1(d). We see that ΔP monotonously increases with λ . Consequently, ΔP effectively measures how far the assumed measurement operators are from the actual ones. Moreover, the shape of the purity landscape is determined by the error vector $\vec{\delta}$. We will leverage this dependence of apparent purity as a function of vector δ to find the true measurement operators.

The method is not limited to the particular reconstruction method, as we illustrate in an example of rotating quarter-wave plate polarimetry with classical Fourier retrieval of Stokes parameters [23]. The example is provided in Supplementary Material S4. In that case, the disagreement between actual and assumed measurement operators causes inconsistency in the tomogram, which results in apparent state-dependent modulation of the degree of polarization, where the degree of polarization can even exceed one.

III. ARTIFACT MITIGATION

We minimize the artifact severity, i.e., purity modulation (5), by varying the measurement operators used to reconstruct the probe states. After recording all tomograms of the probe states we used, we optimize our assumption of $\vec{\delta}$ which specifies the measurement operators used in the reconstruction algorithm. Once the assumed parameters match the actual parameters, the artifact is minimized. Since the perturbed measurement operators no longer add the identity operator, we must properly renormalize them in the reconstruction [22].

Due to the state dependency, the Bloch sphere must be sampled densely enough to detect the mismatch. The probe states should cover the Bloch sphere quasi-uniformly and possess uniform purity; otherwise, their full control is not required. This feature is advantageous in practice because state preparation is never perfect in the experiment. It distinguishes our approach from the schemes that rely on perfect knowledge of the probe states, like quantum measurement tomography [8].

Generally, the optimization landscape has multiple local minima; therefore, global optimization must be performed. Here, we use the NOMAD implementation of

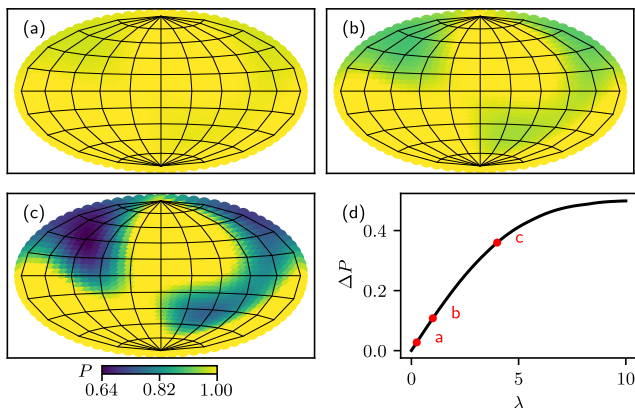


FIG. 1. Purity modulation due to the measurement operator mismatch. (a-c) States are represented as points on the Bloch sphere plotted using Hammer projection, and the purity of their reconstruction is color-coded. Although all probe states were prepared with the same purity, the reconstruction using quantum tomography with mismatched measurement operators yields purity modulation. The purity modulation scales with the magnitude of error parameters. Panel (b) shows the purity modulation for randomly selected error parameters described in the main text. Panels (a) and (c) show how the purity modulation, if we scale the error vector by a factor of $\lambda = 0.25$ and $\lambda = 4$, respectively. The black curve in panel (d) depicts the scaling trend, and red dots on the curve mark the selected values of λ plotted in panels (a-c).

the MADS algorithm [24]. The resulting optimum $\vec{\delta}$ is not unique because any set of measurement operators $\{\hat{U}\hat{\pi}_j\hat{U}^\dagger\}$, where \hat{U} is a fixed unitary operation, also minimizes the artifact. These unitary-equivalent solutions could be interpreted as unitary transformations of probe states. Albeit this ambiguity, such a calibration is already applicable in schemes invariant to local unitaries such as random measurement [25] or entanglement certification [26–28], where only relative orientations of $\hat{\pi}_j$ operators are important. Moreover, the unitary operation can be easily determined by additional measurement of two known and non-orthogonal probe states.

Since the artifact is state-dependent, the probe sampling strategy is important for minimization. The sampling with too few probe states could lead to false error parameters $\vec{\delta}_f$. We found out that 30 quasi-uniformly distributed probe states provide a reliable determination of error parameters in all tested cases. When we used fewer probe states, we encountered incorrect estimates. The incorrect estimate provides reduced apparent purity modulation in the set of probe states, but when it is used on other states, the purity modulation can be even larger than initially.

To test the method numerically, we first randomly generate ground-truth error parameters $\vec{\delta}$. Each element is normally distributed with zero mean value and standard deviation of 10 deg. Then, we produce tomograms corresponding to pure probe states $\rho_k = |\psi_k\rangle\langle\psi_k|$. For simplicity, we exclude statistical noise from our simulations. Parameters $\vec{\delta}$ assumed in the reconstruction are optimized to minimize the purity modulation ΔP in the set of reconstructed probe states $\{\hat{\rho}_k\}$ for $k = 1, \dots, 30$, concluding the calibration step.

To verify the correctness of the optimization result, we use the ground truth $\vec{\delta}$ again to generate tomograms of pure test states $\hat{\xi} = |\xi_k\rangle\langle\xi_k|$, which quasi-uniformly covers the Bloch sphere in 108 points. We reconstruct these states using the optimized parameters $\vec{\delta}$ obtained in the calibration step and calculate the purity of the reconstructions. As a further test, we assume knowledge of two non-orthogonal probe states and use their reconstructions to determine corrective unitary operation \hat{W} . We apply \hat{W} to all reconstructed test states $\hat{\xi}_k$ to eliminate the unitary-related ambiguity. Then, we check their fidelity with the expected ideal test state, $F_k = \text{Tr}[\sqrt{\sqrt{\hat{\xi}_k}\hat{\rho}_k\sqrt{\hat{\xi}_k}}$. We characterize the test states ensemble with the purity modulation and their lowest fidelity $\min_k F_k$ to provide the worst-case estimate.

We repeated the whole numerical simulation 100 times, randomly choosing new ground truth for the error parameters δ in each run. The details about optimizer settings are provided in Section S1 of the Supplementary Material. When we compare the optimized results to the reference, i.e. the states reconstructed with the assumption of null error vector, the average purity modulation decreases from $\Delta P = (8_{-3}^{+3}) \cdot 10^{-2}$ to $\Delta P = (1.0_{-1.0}^{+0.8}) \cdot 10^{-3}$. The

uncertainty interval spans from 0.158 to 0.842-quantile in correspondence to one standard deviation and is used due to the skewed distribution of the results. Mainly, the infidelity decreased from $(3_{-2}^{+1}) \cdot 10^{-2}$ to $(3_{-3}^{+5}) \cdot 10^{-4}$, which represents two orders of magnitude improvement in accuracy. This improvement is crucial for reaching error levels low enough for quantum error correction schemes. The lower ΔP of the probe state ensemble was achieved the better results in the test ensemble we achieved. These results illustrate the feasibility of such optimization and its ability to reliably determine the true measurement operators. It is important to stress that the pure probe states and projective (pure) measurements were chosen here for the simplicity of introducing the measurement-device agnostic framework. However, the method is fully applicable in real cases of generic positive-operator-valued measurements and nonunity purity, as indicated in the following experimental demonstration.

In the multi-qubit scenario, the tomography is usually done using local measurements. In that case, we use the presented method for each local measurement device.

The artifact severity scales worst as $P_{\min,n} = \prod_{i=1}^n P_{\min,i}$ for n -qubit state tomography, where $P_{\min,i}$ is the corresponding minimal purity observed at the single qubit. If the input state $|\psi_i\rangle$ at the i -th qubit suffers from the artifact the most, then product state $\bigotimes_i |\psi_i\rangle$ is the n -qubit state with the greatest manifestation of the artifact. In such a case, the single-qubit improvements multiply and lead to significantly better overall results in multi-qubit scenarios.

IV. STATE PREPARATION

The state preparation typically suffers from imperfections too. Here, we use the symmetry in the Born rule to formally exchange state preparation and measurement to utilize the previously introduced method to correct state preparation. Usually, the qubit is initialized in state $|0\rangle$, then turned into state $|\psi_j\rangle = \hat{U}_j|0\rangle$ by unitary evolution \hat{U}_j . The tomographic projection is also typically realized by some unitary evolution \hat{V}_k and subsequent projection, i.e., $|\pi_k\rangle = \hat{V}_k^\dagger|0\rangle$. The state tomogram of the probe state $|\psi_j\rangle$ consists of measured probabilities $|\langle\hat{\pi}_k|\psi_j\rangle|^2 = |\langle 0|\hat{V}_k\hat{U}_j|0\rangle|^2$. The discussed procedure obtains information related to projections, i.e. about V_k .

Physical reversal of the process consists of preparing states $\hat{V}_k|0\rangle$ and projecting them onto states $\hat{U}_j^\dagger|0\rangle$, obtaining tomogram elements $p_{kj} \propto |\langle 0|\hat{U}_j\hat{V}_k|0\rangle|^2$. We can analyze the tomograms to improve our knowledge of the measurement operator, i.e., $\hat{U}_j^\dagger|0\rangle\langle 0|\hat{U}_j$, related to state preparation in the non-reversed situation. The physical reversal can be realized in the experiment by performing projections onto the original probe states in the tomographic device and preparing states corresponding to the

original tomographical projectors instead of the original probes. Either way, we gain information about \hat{U}_j , increasing the accuracy of state preparation.

V. SPECIAL CASE: MULTIPLICATIVE ERROR

An important subclass of the problem is the case of multiplicative measurement operator error, where

$$\theta'_j = (1 + \delta)\theta_j, \quad (6)$$

$$\phi'_j = (1 + \epsilon)\phi_j. \quad (7)$$

This case is relevant when we sequentially switch the unitary operations that precede a fixed projector to perform the tomographic measurements. These multiplicative errors could be interpreted as Bloch sphere under- or over-rotation. This approach to quantum state tomography has been reported in various platforms, including optics [29, 30], color-centers in solids [31], trapped ions [32], neutral atoms [33], or superconducting qubits [34], making this problem subclass highly relevant.

Because parameters (δ, ϵ) are shared among all projection operators, the optimum search simplifies from 12 parameters to just two. In Section S2 of the Supplementary material, we show that with just eight probe states, the optimization landscape possesses a single minimum, and therefore standard gradient-descent optimization is applicable. The advantage is better performance when compared to global optimization and also the smaller probe state set. Another advantage is that the global optimum is now unique, and the method unambiguously finds the true set $\{\hat{\pi}_j\}$ even when there is an unknown unitary operation between preparation and tomographic measurements.

VI. EXPERIMENT: POLARIZATION STATE TOMOGRAPHY

We experimentally demonstrate the method in the waveplate-based polarization state tomography scenario, an example of a situation with multiplicative errors. At the end of the process, we will improve our knowledge of the waveplate retardance and consequently mitigate the reconstruction artifact.

The experimental setup is depicted in Fig. 1(a). We used a continuous-wave 810 nm thermally-stabilized fiber-coupled laser diode (LD). The laser beam was decoupled into free space using an 11-mm aspheric lens and horizontally polarized using a Glan-Taylor prism (GT). The waveplates HWP1 and QWP1 effectively control the prepared polarization state. The following operator describes the action of a waveplate:

$$\hat{W}_{\alpha,\gamma} = |\alpha\rangle\langle\alpha| + e^{-i\Gamma}|\alpha_\perp\rangle\langle\alpha_\perp|, \quad (8)$$

where α and Γ are its angular position and retardance, and $|\alpha\rangle = \cos\alpha|0\rangle + \sin\alpha|1\rangle$ is a linearly polarized state,

and $\alpha_\perp = \alpha + \pi/2$. To prepare a state located at colatitude θ and longitude ϕ on the Bloch sphere, we rotate the half- and quarter-wave plate to angles x' and y' given by the relations

$$y' = -\frac{1}{2} \arcsin(\sin\theta \sin\phi), \quad (9)$$

$$x' = \frac{1}{4} \arctan(\tan\theta \cos\phi) + \frac{1}{2}y + c(\theta), \quad (10)$$

where $c(\theta) = \pi/4$ if $\theta > \pi/2$ and $c(\theta) = 0$ otherwise. This relation holds for wave plates that have perfect retardance. The deviation from the ideal retardance will introduce errors in the preparation. We assumed the perfect retardance in the first step of the experiment as our method does not require exact knowledge of probe states.

To demonstrate the tolerance of the method to a unitary operation between preparation and tomographic measurement, we add a quarter-wave plate (QWPX) with its fast axis oriented at -12.5 deg relative to the horizontal direction. Because this unitary operation can be in principle unknown, we restrict ourselves from using any information about QWPX in the calibration.

The states were analyzed using half-waveplate and quarter-wave (HWP2, QWP2) and subsequent projection onto horizontal and vertical polarization using a calcite beam-displacer (BD). The waveplate settings for the Pauli tomography are listed in Tab. S2 of the Supplementary Material. All waveplates were mounted into a precision motorized rotation stage that provided bidirectional repeatability of ± 30 mdeg.

We used reverse-biased PIN photodiodes (PD) to measure optical intensity at both outputs of the beam-displacer. We normalized the readings using the sum of two signals to eliminate laser power fluctuation.

The action of the waveplate could be seen as the rotation of the Bloch sphere around axis $(\sin(2\alpha), 0, \cos(2\alpha))$ with rotation angle Γ , where α determines the angular position of the waveplate and Γ its retardance. The retardance usually slightly deviates from its nominal value. These deviations manifest as under- or over-rotation of the Bloch sphere. We parameterize the measurement operator by precisely controlled waveplate angular positions x , y , and half- and quarter-wave plate retardance deviations δ and ϵ , respectively. These deviations are initially unknown to us, and we will use the presented method to estimate their values.

We use eight probe states and perform the Pauli tomography for each. Initially, we assume zero deviations, $\delta = \epsilon = 0$, and observe the purity modulation $\Delta P = 0.0572(3)$. The number in parenthesis is one standard deviation at the last significant digit, e.g. $0.0572(3) = (572 \pm 3) \cdot 10^{-4}$. The uncertainties were estimated using bootstrapping with the assumption of normally distributed photo-current with 0.1% relative standard deviation, which is the most dominant term and is related to the ammeter precision. The shot noise is negligible at the power level of our laser, compared to the technical noise. Then, we vary parameters δ and

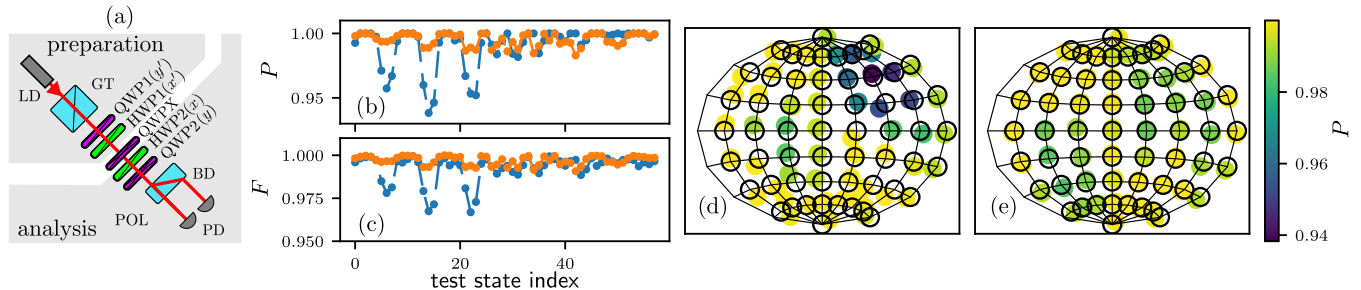


FIG. 2. Experimental demonstration for a polarization-encoded photonic qubit. Panel (a) shows the experimental scheme: LD - laser diode, HWP (QWP) - half-(quarter)-wave plate, GT - Glan-Taylor polarizer, BD - calcite beam displacer, PD - photodiode. Panels (b) and (c) show the purity and fidelity of reconstructed test states before (blue) and after (orange) application of measurement-device agnostic calibration. The fidelity of reconstructed states is calculated with respect to theoretical test states. The theoretical test states are depicted as empty black circles on the projected Bloch sphere in panels (d, e). Panel (d) depicts the reference case – the method was not used, and we assumed perfect waveplates in preparation and tomographic projections. In contrast, panel (e) shows the improved precision of preparation and measurement when we use the method and take into account the retardance deviation. The purity modulation is reduced and the test states match closely the theoretical expectations. In both panels, the reconstructed states are represented on the Bloch sphere using Hammer projection, and their purity is color-coded.

ϵ and update the measurement operators employed in the reconstruction to minimize the purity modulation. The optimal δ and ϵ are close to the true values because the reconstruction artifact is significantly reduced to $\Delta P = 0.0140(2)$. We found the optimal parameters $\delta = 4.5(2)$ deg, $\epsilon = -1.30(4)$ deg.

We then reverse the process to determine retardance deviations $\tilde{\delta}, \tilde{\epsilon}$ of the waveplates used in state preparation. We prepare the six eigenstates of Pauli operators, project each onto eight states corresponding to the original probe state set, and treat this data as before. We minimize the apparent purity modulation from $0.0700(3)$ to $0.0144(2)$ to find the optimal parameters $\tilde{\delta} = 4.53(6)$ deg and $\tilde{\epsilon} = -3.58(3)$ deg.

The calibration step revealed the retardance deviation of the wave plates used for preparation and projection. To reconstruct the quantum states, we could directly use this knowledge to update our measurement operators. However, we take one extra step which allows us to prepare the states with greater precision and control the measurement operators precisely. We took these deviations into account in the verification step and calculated new angular positions of wave plates for tomographic projections and state preparation. Since Eq. 10 does not hold anymore, we used numerical optimization to find the desired wave plate settings (x, y) :

$$x, y = \operatorname{argmax}_{x,y} |\langle \psi | \hat{W}(x, \pi + \delta) \hat{W}(y, \pi/2 + \epsilon) | 0 \rangle|^2. \quad (11)$$

Similarly, to find the settings to project a state onto state $|\pi\rangle$ we perform this maximization

$$x, y = \operatorname{argmax}_{x,y} |\langle 0 | \hat{W}(x, \pi/2 + \epsilon) \hat{W}(y, \pi + \delta) | \pi \rangle|^2. \quad (12)$$

At this point, we have information about actual measurement operators, and we have also calibrated the state

preparation. This calibration was done in the presence of a unitary operation between state preparation and measurement, which was introduced by QWPX. This operation was effectively unknown because we did not use any prior information about QWPX during the process.

Now, we proceed to certify the correctness of such a calibration. The calibration should remain valid even if we change the central unitary operation introduced by QWPX. To test this, we removed the QWPX and then prepared an ensemble of 58 test states, depicted as empty circles in Figure 2(c,d).

As a reference, we first assumed perfect waveplates and performed state tomography for each test state. We indeed observed purity modulation $\Delta P = 0.0607(2)$ with purity minimum $P_{\min} = 0.9383(2)$. This modulation indicates reconstruction artifacts. The minimum fidelity of the reconstructed state to the target states was $F_{\min} = 0.96688(4)$. These fidelity values indicate imprecise preparation.

In contrast, when we used our knowledge of δ and ϵ in the reconstruction and preparation, the minimum purity increased to $0.9830(3)$ and the minimum fidelity to $F_{\min} = 0.9907(2)$. The information gained in the calibration clearly improved the reconstruction.

The results in Figure 2 indicate improved quality of state preparation and tomographic measurements when we use the knowledge of δ and ϵ to improve both preparation and measurement. The small remaining artifacts are present due to the limited precision of the learned retardance deviations and also the repeatability of the waveplate rotation.

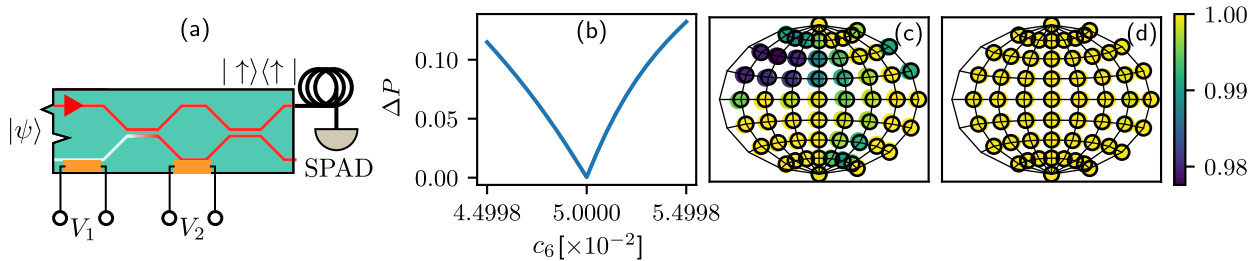


FIG. 3. Application of the method for on-chip photonic path qubit. (a) Projection apparatus for a path qubit. Applied voltage $V_{1,2}$ on heater elements (orange) causes thermal-based phase shift in the waveguide interferometers. These shifts determine the measurement projector. The photons in the upper output path are detected with a single-photon detector (SPAD). (b) 1D-section of 6D function $\Delta P(c_1, \dots, c_6)$. The value of ΔP at the initial assumption of c_j is $1.8 \cdot 10^{-2}$ on the ensemble of probe states. Minimum $\Delta P = 4.5 \cdot 10^{-4}$ lies at the true value c'_6 . (c) Initial mismatch results in state-dependent purity artifact. We plot test states on the Bloch sphere as circles and color-code their reconstructed purity. (d) When we consider the true retardance, the artifact vanishes.

VII. PATH-ENCODED QUBITS ON A PHOTONIC CHIP

As another example, we numerically illustrate the measurement-device agnostic calibration for tomography of photonic on-chip path qubits [30, 35–37]. The qubit is encoded into the photon propagation in one or another waveguide (states $|\uparrow\rangle$ or $|\downarrow\rangle$), as depicted in Figure 3(a). The local heating of one waveguide controls the phase between the two paths. The heating is typically achieved by an electrical current flowing through a small heater element. A Mach-Zehnder interferometer serves as a variable coupler, and its interferometric phase controls the coupling ratio. Detection of photons in a single optical path implements a projective measurement of the path qubit. The circuit in Figure 3(a) implements a projection onto state $|\pi\rangle$, whose colatitude and longitude on the Bloch sphere are controlled by optical phases. The relation between optical phases $\varphi_{1,2}$ and voltages $V_{1,2}$ applied on the heating elements is approximated with polynomials [35]

$$\varphi_1(V_1) = c_1 + c_2 V_1 + c_3 V_1^2, \quad (13)$$

$$\varphi_2(V_2) = c_4 + c_5 V_2 + c_6 V_2^2. \quad (14)$$

$$(15)$$

Here, the voltages $V_{1,2}$ are controlled perfectly, but parameters c_j are known only approximately. The other imperfections are neglected. We have increased the number of probe states to 22 to compensate for the higher number of optimization parameters. The simulated experiment, depicted in Fig. 3(c), shows the measurement operator mismatch artifact. We search the six-dimensional parametric space to find the point of minimal $\Delta P(c_j)$ where the systematic error is mitigated. Panel (b) shows a one-dimensional section illustrating that the minimal ΔP corresponds to the true value c'_6 . Taking the true values c'_j into account mitigates the reconstruction artifact, as shown in panel (d).

VIII. CONCLUSION

The mismatch between actual measurement operators and their theoretical counterparts assumed in reconstructing quantum states or devices introduces reconstruction artifacts. We showed how to leverage these artifacts to reveal the actual measurement operators and mitigate systematic errors in the tomography and state preparation. We experimentally applied this method to Pauli tomography of polarization-encoded photonic qubits and numerically analyzed several other measurement schemes. The proposed method makes the tomography independent of the measurement device. The main advantage is that the method does not require perfect knowledge or control of the probe states, which is virtually impossible to obtain. The method can calibrate already existing tomographic apparatus without the need for individual characterization of its constituent components. This is particularly useful in the case where the experimental setup is monolithic and individual components cannot be calibrated individually, e.g. in the case of integrated circuits. One can also calibrate the state preparation using the same method. Furthermore, the presented approach applies locally to individual parties of a larger multiparty system; i.e. it is fully scalable.

In summary, we developed the framework for accurate and scalable calibration of quantum measurement devices and also quantum state preparation, which is critical in any applications of quantum science and technology.

The application of the reported measurement-device agnostic quantum measurement goes beyond the full quantum tomography [13, 22]. The same method will find its use for mitigation of measurement errors in various approximative and more scalable approaches such as Monte-Carlo sampling [38–41], permutationally invariant tomography [42], compressed sensing [43, 44], etc. The method can also improve the accuracy of building and characterization of the photonic and quantum circuits in complex media [45, 46]. Finally, the reported approach

also applies to experimental realizations of entanglement certification and quantification [25–28, 47].

The supporting data for this article are available from the Zenodo repository [48].

ACKNOWLEDGMENTS

We acknowledge the support of the Czech Science Foundation under grant No. 21-18545S. M. B. acknowl-

edges the support of Palacký University under grant No. IGA-PrF-2024-008. We acknowledge the use of cluster computing resources provided by the Department of Optics, Palacký University Olomouc. We thank J. Provazník for maintaining the cluster and providing support.

-
- [1] M. A. Nielsen and I. L. Chuang, *Quantum Computation and Quantum Information: 10th Anniversary Edition* (Cambridge University Press, 2010).
- [2] G. M. D’Ariano, M. G. A. Paris, and M. F. Sacchi, Quantum tomography, *Adv. Imaging Electron Phys.* **128**, 205 (2003).
- [3] M. Paris and J. Řeháček, *Quantum State Estimation* (Springer, Berlin, Germany, 2004).
- [4] Y. S. Teo, *Introduction to quantum-state estimation* (World Scientific, 2015).
- [5] J. Eisert, D. Hangleiter, N. Walk, I. Roth, D. Markham, R. Parekh, U. Chabaud, and E. Kashefi, Quantum certification and benchmarking, *Nature Reviews Physics* **2**, 382 (2020).
- [6] V. Gebhart, R. Santagati, A. A. Gentile, E. M. Gauger, D. Craig, N. Ares, L. Bianchi, F. Marquardt, L. Pezzè, and C. Bonato, Learning quantum systems, *Nature Reviews Physics* **5**, 141 (2023).
- [7] J. Fiurášek, Maximum-likelihood estimation of quantum measurement, *Phys. Rev. A* **64**, 024102 (2001).
- [8] J. S. Lundeen, A. Feito, H. Coldenstrodt-Ronge, K. L. Pregnell, C. Silberhorn, T. C. Ralph, J. Eisert, M. B. Plenio, and I. A. Walmsley, Tomography of quantum detectors, *Nature Physics* **5**, 27 (2008).
- [9] G. Brida, L. Ciavarella, I. P. Degiovanni, M. Genovese, A. Migdall, M. G. Mingolla, M. G. A. Paris, F. Piacentini, and S. V. Polyakov, Ancilla-assisted calibration of a measuring apparatus, *Phys. Rev. Lett.* **108**, 253601 (2012).
- [10] G. Brida, L. Ciavarella, I. P. Degiovanni, M. Genovese, L. Lolli, M. G. Mingolla, F. Piacentini, M. Rajteri, E. Taralli, and M. G. A. Paris, Quantum characterization of superconducting photon counters, *New J. Phys.* **14**, 085001 (2012).
- [11] D. Mogilevtsev, J. Řeháček, and Z. Hradil, Self-calibration for self-consistent tomography, *New Journal of Physics* **14**, 095001 (2012).
- [12] A. M. Brańczyk, D. H. Mahler, L. A. Rozema, A. Darabi, A. M. Steinberg, and D. F. V. James, Self-calibrating quantum state tomography, *New Journal of Physics* **14**, 085003 (2012).
- [13] M. Ježek, J. Fiurášek, and Z. Hradil, Quantum inference of states and processes, *Phys. Rev. A* **68**, 012305 (2003).
- [14] A. C. Keith, C. H. Baldwin, S. Glancy, and E. Knill, Joint quantum-state and measurement tomography with incomplete measurements, *Phys. Rev. A* **98**, 042318 (2018).
- [15] I. Roth, J. Wilkens, D. Hangleiter, and J. Eisert, Semi-device-dependent blind quantum tomography, *Quantum* **7**, 1053 (2023).
- [16] A. Jamiolkowski, Linear transformations which preserve trace and positive semidefiniteness of operators, *Reports on Mathematical Physics* **3**, 275 (1972).
- [17] M.-D. Choi, Completely positive linear maps on complex matrices, *Linear Algebra and its Applications* **10**, 285 (1975).
- [18] M. D. de Burgh, N. K. Langford, A. C. Doherty, and A. Gilchrist, Choice of measurement sets in qubit tomography, *Phys. Rev. A* **78**, 052122 (2008).
- [19] Y. I. Bogdanov, G. Brida, M. Genovese, S. P. Kulik, E. V. Moreva, and A. P. Shurupov, Statistical estimation of the efficiency of quantum state tomography protocols, *Phys. Rev. Lett.* **105**, 010404 (2010).
- [20] J. Řeháček, Y. S. Teo, and Z. Hradil, Determining which quantum measurement performs better for state estimation, *Phys. Rev. A* **92**, 012108 (2015).
- [21] H. Sosa-Martinez, N. K. Lysne, C. H. Baldwin, A. Kalev, I. H. Deutsch, and P. S. Jessen, Experimental study of optimal measurements for quantum state tomography, *Phys. Rev. Lett.* **119**, 150401 (2017).
- [22] Z. Hradil, J. Řeháček, J. Fiurášek, and M. Ježek, Maximum-likelihood methods in quantum mechanics, in *Quantum State Estimation*, edited by M. Paris and J. Řeháček (Springer Berlin Heidelberg, Berlin, Heidelberg, 2004) pp. 59–112.
- [23] D. Goldstein and D. Goldstein, *Polarized Light, Revised and Expanded*, Optical engineering (CRC Press, 2003).
- [24] C. Audet, S. L. Digabel, V. R. Montplaisir, and C. Tribes, Nomad version 4: Nonlinear optimization with the mads algorithm, *ACM Transactions on Mathematical Software* **48**, 1 (2022).
- [25] A. Elben, S. T. Flammia, H.-Y. Huang, R. Kueng, J. Preskill, B. Vermersch, and P. Zoller, The randomized measurement toolbox, *Nature Reviews Physics* **5**, 9–24 (2022).
- [26] N. Friis, G. Vitagliano, M. Malik, and M. Huber, Entanglement certification from theory to experiment, *Nature Reviews Physics* **1**, 72–87 (2018).
- [27] N. Herrera Valencia, V. Srivastav, M. Pivoluska, M. Huber, N. Friis, W. McCutcheon, and M. Malik, High-Dimensional Pixel Entanglement: Efficient Generation and Certification, *Quantum* **4**, 376 (2020).
- [28] N. Wyderka, A. Ketterer, S. Imai, J. L. Bönsel, D. E. Jones, B. T. Kirby, X.-D. Yu, and O. Gühne, Complete characterization of quantum correlations by randomized measurements, *Phys. Rev. Lett.* **131**, 090201 (2023).
- [29] K. J. Resch, P. Walther, and A. Zeilinger, Full characterization of a three-photon greenberger-horne-zeilinger

- state using quantum state tomography, *Phys. Rev. Lett.* **94**, 070402 (2005).
- [30] P. J. Shadbolt, M. R. Verde, A. Peruzzo, A. Politi, A. Laing, M. Lobino, J. C. F. Matthews, M. G. Thompson, and J. L. O'Brien, Generating, manipulating and measuring entanglement and mixture with a reconfigurable photonic circuit, *Nature Photonics* **6**, 45 (2011).
- [31] J. Zhang, S. S. Hegde, and D. Suter, Fast quantum state tomography in the nitrogen vacancy center of diamond, *Phys. Rev. Lett.* **130**, 090801 (2023).
- [32] V. Krutyanskiy, M. Galli, V. Krcmarsky, S. Baier, D. A. Fioretto, Y. Pu, A. Mazloom, P. Sekatski, M. Canteri, M. Teller, J. Schupp, J. Bate, M. Meraner, N. Sangouard, B. P. Lanyon, and T. E. Northup, Entanglement of trapped-ion qubits separated by 230 meters, *Phys. Rev. Lett.* **130**, 050803 (2023).
- [33] A. Noguchi, Y. Eto, M. Ueda, and M. Kozuma, Quantum-state tomography of a single nuclear spin qubit of an optically manipulated ytterbium atom, *Phys. Rev. A* **84**, 030301 (2011).
- [34] M. Steffen, M. Ansmann, R. C. Bialczak, N. Katz, E. Lucero, R. McDermott, M. Neeley, E. M. Weig, A. N. Cleland, and J. M. Martinis, Measurement of the entanglement of two superconducting qubits via state tomography, *Science* **313**, 1423 (2006).
- [35] J. Carolan, C. Harrold, C. Sparrow, E. Martín-López, N. J. Russell, J. W. Silverstone, P. J. Shadbolt, N. Matsuda, M. Oguma, M. Itoh, G. D. Marshall, M. G. Thompson, J. C. F. Matthews, T. Hashimoto, J. L. O'Brien, and A. Laing, Universal linear optics, *Science* **349**, 711 (2015).
- [36] F. Flamini, L. Magrini, A. S. Rab, N. Spagnolo, V. D'Ambrosio, P. Mataloni, F. Sciarrino, T. Zandrini, A. Crespi, R. Ramponi, and R. Osellame, Thermally reconfigurable quantum photonic circuits at telecom wavelength by femtosecond laser micromachining, *Light Sci. Appl.* **4**, 10.1038/lssa.2015.127 (2015).
- [37] C. Taballione, M. C. Anguita, M. de Goede, P. Venderbosch, B. Kassenberg, H. Sniijders, N. Kannan, W. L. Vleeshouwers, D. Smith, J. P. Epping, R. van der Meer, P. W. H. Pinkse, H. van den Vlekkert, and J. J. Renema, 20-Mode Universal Quantum Photonic Processor, *Quantum* **7**, 1071 (2023).
- [38] S. T. Flammia and Y.-K. Liu, Direct fidelity estimation from few pauli measurements, *Phys. Rev. Lett.* **106**, 230501 (2011).
- [39] M. Mičuda, M. Sedlák, I. Straka, M. Miková, M. Dušek, M. Ježek, and J. Fiurášek, Efficient experimental estimation of fidelity of linear optical quantum toffoli gate, *Physical Review Letters* **111**, 10.1103/physrevlett.111.160407 (2013).
- [40] R. Stárek, M. Mičuda, M. Miková, I. Straka, M. Dušek, M. Ježek, and J. Fiurášek, Experimental investigation of a four-qubit linear-optical quantum logic circuit, *Scientific Reports* **6**, 10.1038/srep33475 (2016).
- [41] M. Mičuda, M. Miková, I. Straka, M. Sedlák, M. Dušek, M. Ježek, and J. Fiurášek, Tomographic characterization of a linear optical quantum toffoli gate, *Physical Review A* **92**, 10.1103/physreva.92.032312 (2015).
- [42] G. Tóth, W. Wieczorek, D. Gross, R. Krischek, C. Schwemmer, and H. Weinfurter, Permutationally invariant quantum tomography, *Phys. Rev. Lett.* **105**, 250403 (2010).
- [43] D. Gross, Y.-K. Liu, S. T. Flammia, S. Becker, and J. Eisert, Quantum state tomography via compressed sensing, *Phys. Rev. Lett.* **105**, 150401 (2010).
- [44] C. A. Riofrío, D. Gross, S. T. Flammia, T. Monz, D. Nigg, R. Blatt, and J. Eisert, Experimental quantum compressed sensing for a seven-qubit system, *Nature Communications* **8**, 10.1038/ncomms15305 (2017).
- [45] S. Leedumrongwatthanakun, L. Innocenti, H. Defienne, T. Juffmann, A. Ferraro, M. Paternostro, and S. Gigan, Programmable linear quantum networks with a multi-mode fibre, *Nature Photonics* **14**, 139–142 (2019).
- [46] S. Goel, S. Leedumrongwatthanakun, N. H. Valencia, W. McCutcheon, A. Tavakoli, C. Conti, P. W. H. Pinkse, and M. Malik, Inverse design of high-dimensional quantum optical circuits in a complex medium, *Nature Physics* **20**, 232–239 (2024).
- [47] D. Koutný, L. Ginés, M. Moczala-Dusanowska, S. Höfling, C. Schneider, A. Predojević, and M. Ježek, Deep learning of quantum entanglement from incomplete measurements, *Sci. Adv.* **9**, 10.1126/sciadv.add7131 (2023).
- [48] R. Stárek, Zenodo repository <https://doi.org/10.5281/zenodo.11348290> (2024).

Measurement-device agnostic quantum tomography – Supplementary material

Robert Stárek,* Martin Bielak, and Miroslav Ježek

Department of Optics, Faculty of Science, Palacký University, 17. listopadu 12, 77146 Olomouc, Czechia

S1. NOMAD SETTING IN THE NUMERICAL TEST

When we numerically investigated the case of general additive errors, we set the NOMAD [1] parameters as listed in Tab. S1. Please refer to the NOMAD 4 manual [2] for the meaning of the parameters. The optimized parameters were bounded to the interval $(-29, 29)$ deg, i.e., roughly three standard deviations of the true parameter distribution. The seed was pseudo-randomly chosen at the time of optimization. The maximum size of the evaluation block was set as twice the problem dimension to allow optimal parallelization of the initial Latin hypercube search. We used the *nomadlad* [3] package to use NOMAD from Python. The necessary configuration was to set NOMAD to use multiple initial optimization points instead of just one by not specifying parameter X0 and setting the Latin hypercube search parameter (LH SEARCH) sufficiently high.

S2. ARTIFACT MITIGATION OF MULTIPLICATIVE ERRORS

Here, we explore the sampling strategies in the case of multiplicative errors. Since the artifact is state-dependent, the probe sampling strategy is important for minimizing the reconstruction artifacts.

As in the main text, all states are measured in projections onto eigenstates of Pauli operators. The projections are implemented by rotating the measured state using the following unitary operation $\hat{R}_y(\theta_j)\hat{R}_z(\phi_j)$ and subsequent projection of the resulting state onto state $|0\rangle$. The rotation angles θ_j, ϕ_j determine the selected projection and are listed in Tab S2.

We test a few sampling schemes and plot the cost function near the ground truth ($\delta' = 0.02, \epsilon' = -0.04$) for each. The cost function is the peak-to-valley value of reconstructed probe state purities, $\Delta P = P_{\max} - P_{\min}$. The probe sets and cost functions are depicted in Figure S1. As probe states set, we selected eigenstates of Pauli operators (panels a,b), eight states in (panels c, d), icosahedron (panels e, f), and then a uniform sampling of Bloch sphere angular coordinates (θ, ϕ) with 14 states (panels g, h) and 22 states (panels i, j) and finally NASA HEALPIX [4, 5] with 108 probe states (panels k, l).

The sampling is sufficient when the cost function possesses a unique global minimum. We have run additional

parameter	value
BB OUTPUT TYPE	OBJ
DIMENSION	12
BB MAX BLOCK SIZE	24
MAX BB EVAL	100 000
SEED	random integer
DIRECTION TYPE	ORTHO 2N
LH SEARCH	1100 1100
LOWER BOUND	$(-0.5, \dots, -0.5)$
UPPER BOUND	$(0.5, \dots, 0.5)$

TABLE S1. NOMAD (v4.1.0) settings used for the global optimization. Some parameters are not listed because they are not critical for this application.

simulations, varied the ground truth, and observed the shape of the cost function. We tested each sampling scheme from Fig. S1. We sampled the cost function near the varying ground truth values of δ' and ϵ' and plotted its value as color maps, depicted in Fig. S1. The first suitable sampling scheme appears for eight probe states. Interestingly, for 14 probe states, there is a rift in the cost function landscape that causes ambiguity in the δ, ϵ determination. The remaining sampling schemes exhibit a well-defined global minimum and therefore are suitable. The cost function landscapes in Fig. S1 are plotted for a single choice of (δ, ϵ) . To better characterize the sampling strategies, we repeated the same simulations for multiple ground truths. Figures S2-S6 show the simulated cost function for 8, 12, 17, 22, and 108 probe states. The ground truth is always plotted in the panel center. This additional characterization confirms the result – 8 probe states are enough and there is indeed anomalous behavior for 14 probe states. For 22 states, we sometimes see a local minimum, such as for ground truth parameters $\delta' = 0.15, \epsilon' = 0$. Due to this, the optimization has to be done carefully, ideally with several starting points, to find the global minimum of the cost function. In the case of 108 probe states, the cost function always had a single minimum.

The most interesting outcome of this analysis is that the success of the sampling strategy is not determined by the sheer number of probe states but rather by their suit-

j	1	2	3	4	5	6
θ_j (y -axis)	0	π	$\pi/2$	$\pi/2$	$\pi/2$	$\pi/2$
ϕ_j (z -axis)	0	0	π	0	$\pi/2$	$3\pi/2$

TABLE S2. Rotation angles in radians for Pauli tomography. The analyzed state is first rotated by ϕ_j around the z -axis and θ_j around the y -axis and subsequently projected to state $|0\rangle$.

* starek@optics.upol.cz

state j	$ H\rangle$ 1	$ V\rangle$ 2	$\frac{ H\rangle+ V\rangle}{\sqrt{2}}$ 3	$\frac{ H\rangle- V\rangle}{\sqrt{2}}$ 4	$\frac{ H\rangle+i V\rangle}{\sqrt{2}}$ 5	$\frac{ H\rangle-i V\rangle}{\sqrt{2}}$ 6
x_j (HWP)	0	$\pi/4$	$\pi/8$	$-\pi/8$	$-\pi/8$	$\pi/8$
y_j (QWP)	0	0	0	0	$-\pi/4$	$\pi/4$
x'_j (HWP)	0	$\pi/4$	$\pi/8$	$-\pi/8$	$\pi/8$	$-\pi/8$
y'_j (QWP)	0	0	0	0	$\pi/4$	$-\pi/4$

TABLE S3. Waveplate angular position for Pauli tomography. The waveplates are placed as follows in the direction of the light propagation: quarter-wave plate and half-wave plate in the preparation, and half-wave plate and quarter-wave plate in the measurement stage. Primed symbols correspond to the state preparation, used in the reversed version of the method.

able placement on the Bloch sphere. Generally, adding more probe states makes the error parameters determination more robust because we increase the obtained information, however, at the cost of longer measurement time. The exact cost function shape, sampling strategies, and shapes of the purity modulation depend on the imperfection type, its parameterization, and how we switch the measurement operators in the tomography.

S3. ROTATING WAVEPLATE POLARIMETRY

Consider the classical rotating quarter-wave plate polarimeter [6], depicted in Fig. S7(a), with the quarter-

wave plate having the true retardance deviated by $\delta' = 5$ deg from its nominal value. Moreover, consider pure probe states. The waveplate rotates continuously and effectively modulates the optical signal detected after the polarizer. Instead of likelihood maximization, we now use classical Fourier analysis to reconstruct the polarization state. We chose the Fourier analysis to show that our method is not limited to maximal likelihood reconstruction. We used eight probe states to detect the reconstruction artifact, and instead of purity modulation, we equivalently measured the severity with a modulation amplitude of the degree of polarization.

First, we treat the data with the ideal retardance ($\delta = 0$) assumption. We see that the states from the ensemble suffer from artifacts. Here, we look at the intensity-

normalized Stokes vector length $D = \frac{\sqrt{\sum_{i=x,y,z} S_i}}{S_0}$, which is proportional to purity $P = \frac{1}{2}(1 + D^2)$. Near state $|H\rangle$, at the north pole of the Bloch sphere, the purity even exceeds 1 due to the reconstruction method. The modulation of D is depicted in Fig. S7(c). This behavior is clearly a reconstruction artifact. Exceeding the unit purity is unsurprising because Fourier analysis does not guarantee physically sound results. We now vary δ assumed in reconstruction and observe the peak-to-peak value ΔD in the probe set. The dependence is depicted in Fig. S7(b). We see that the minimum lies at the true δ' . In panel (d), we show that the artifact disappears when the retardance deviation is taken into account.

-
- [1] C. Audet, S. L. Digabel, V. R. Montplaisir, and C. Tribes, Nomad version 4: Nonlinear optimization with the mads algorithm, *ACM Transactions on Mathematical Software* **48**, 1 (2022).
- [2] C. Audet, S. L. Digabel, V. R. Montplaisir, and C. Tribes, Nomad 4 used guide, <https://nomad-4-userguide.readthedocs.io>.
- [3] J. Provazník, Nomadlad interface, <https://github.com/jan-provaznik/nomadlad> (2022).
- [4] K. M. Gorski, E. Hivon, A. J. Banday, B. D. Wandelt, F. K. Hansen, M. Reinecke, and M. Bartelmann, HEALPix: A framework for high-resolution discretization and fast analysis of data distributed on the sphere, *The Astrophysical Journal* **622**, 759 (2005).
- [5] D. P. Hardin, T. J. Michaels, and E. B. Saff, A comparison of popular point configurations on \mathbf{S}^2 (2016), arXiv:1607.04590 [math.NA].
- [6] D. Goldstein and D. Goldstein, *Polarized Light, Revised and Expanded*, Optical engineering (CRC Press, 2003).

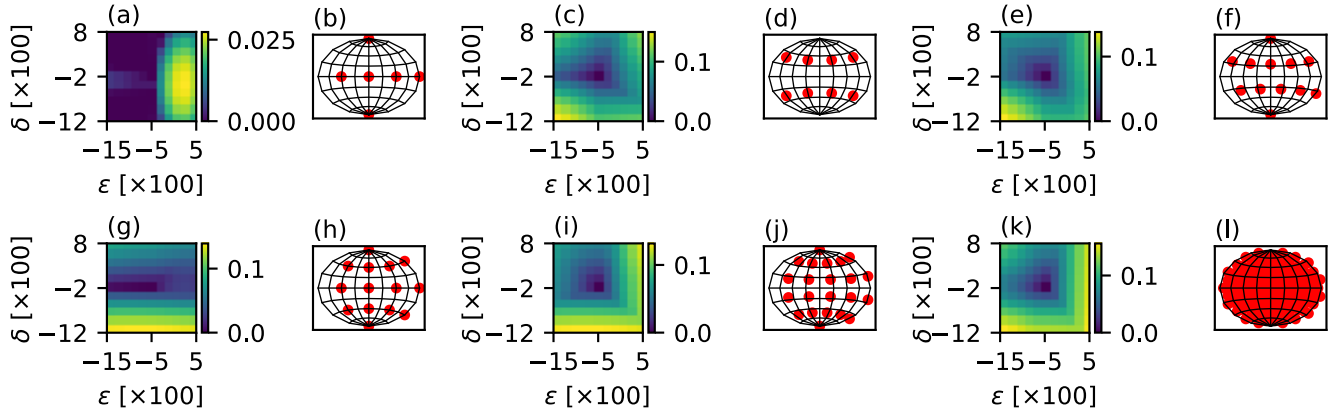


FIG. S1. Dependence of simulated artifact severity, represented as purity modulation amplitude depicted as 2D color maps in panels (a, c, . . . , k) on the selection of probe states set, depicted as points on projected Bloch sphere in panels (b, d, . . . , l). The figure shows the case for 6 (a,b), 8 (c,d), 12 (e,f), 14 (g,h), 22 (i,j), and 108 (k,l) probe states. The purity modulation amplitude is always plotted around the ground truth $\delta = 0.02$, $\delta = -0.04$.

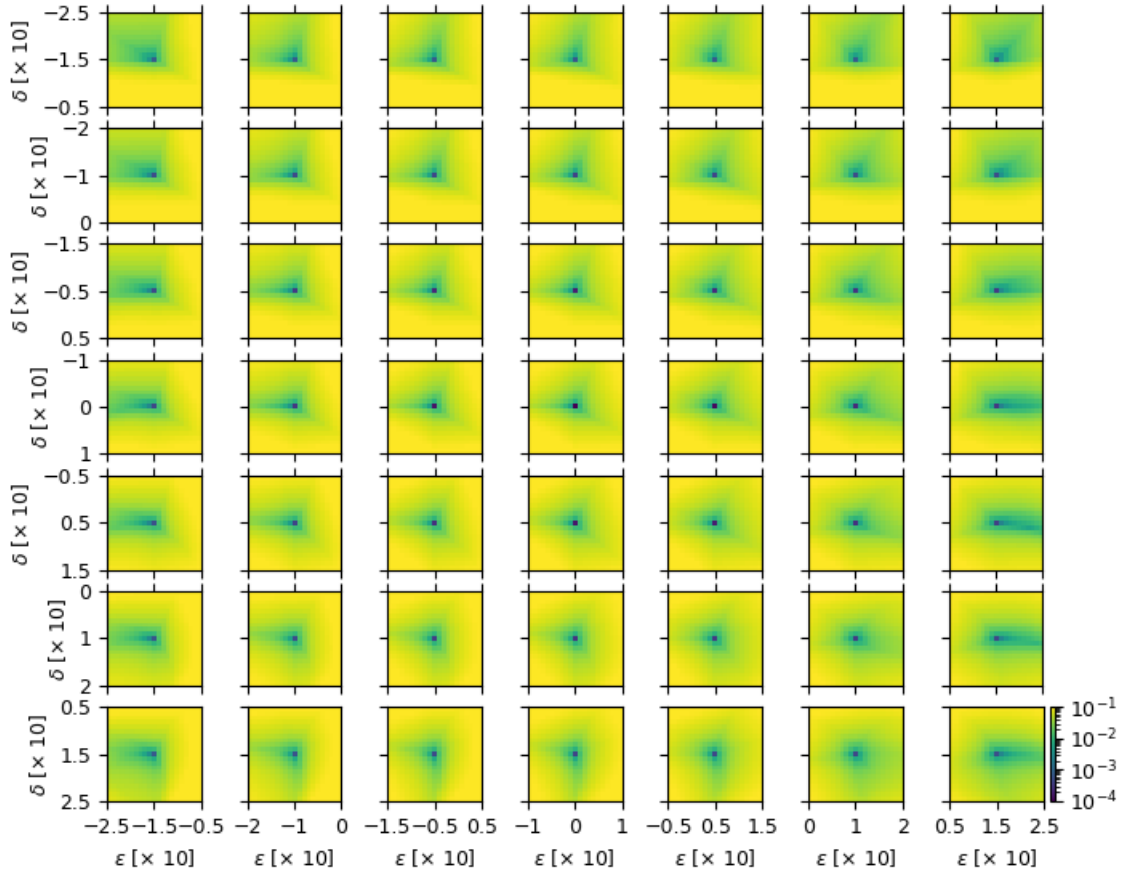


FIG. S2. The panels show color-coded purity modulation as a function of assumed error parameters (δ, ϵ) observed in the set of eight reconstructed probe states. The purity modulation is sampled near the true value (δ', ϵ') for each simulated ground truth. This true value is always plotted in the center of the panel. All panels share the color bar. To visually emphasize the presence of a single minimum, we use logarithmic normalization of color coding.

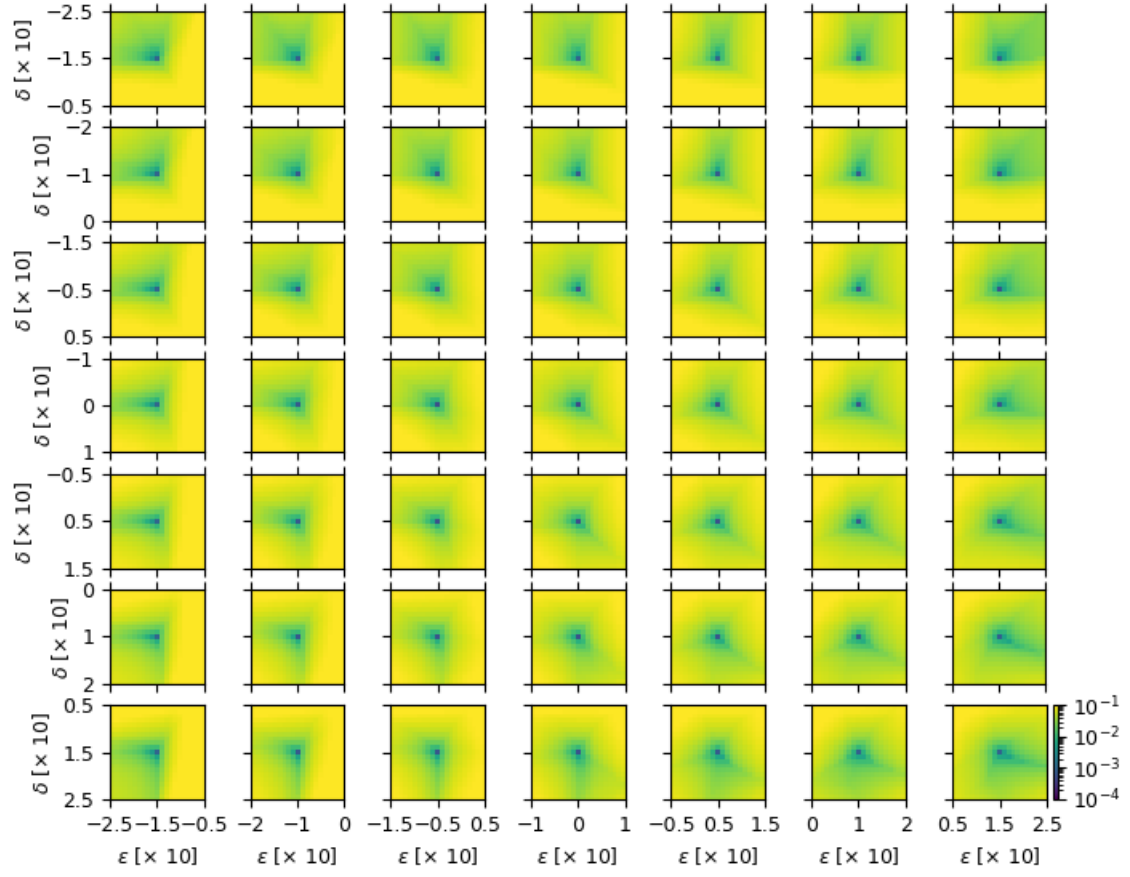


FIG. S3. 12 probe states. The figure is arranged as Fig. S2.

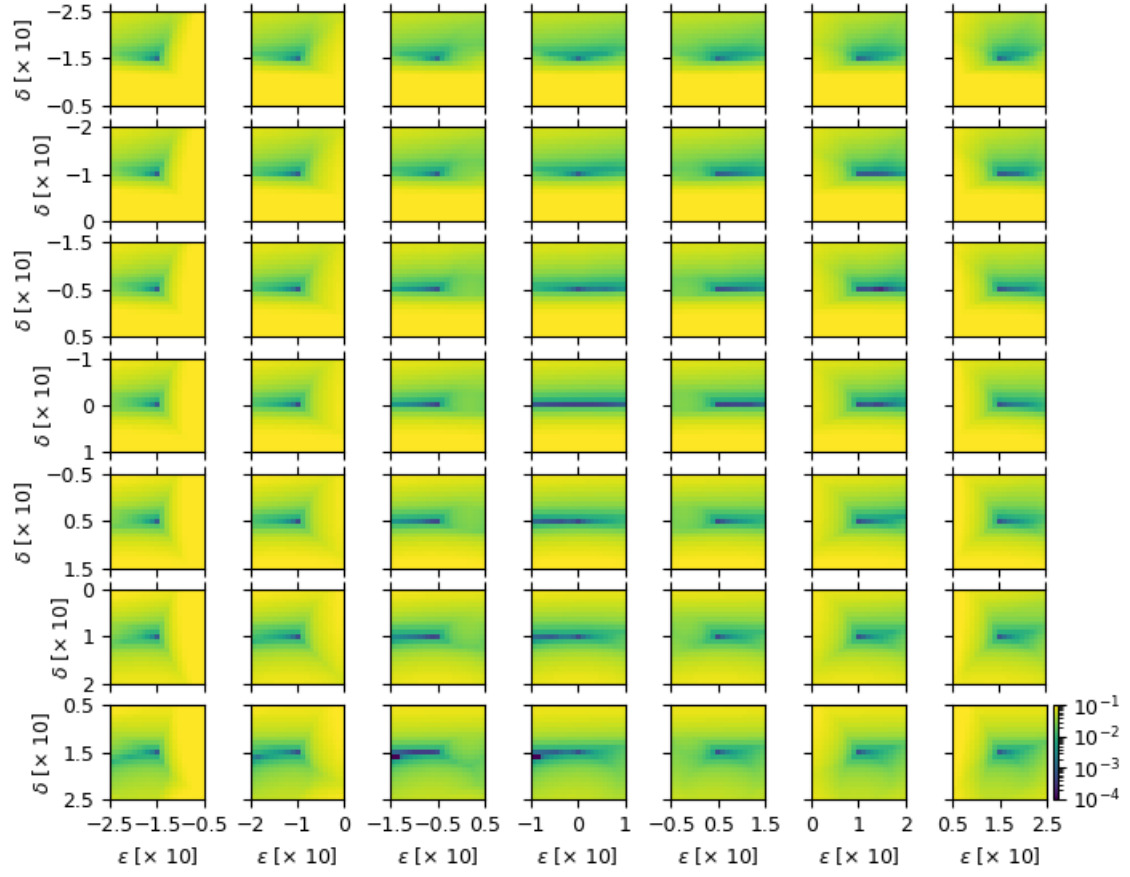


FIG. S4. 14 probe states. The figure is arranged as Fig. S2.

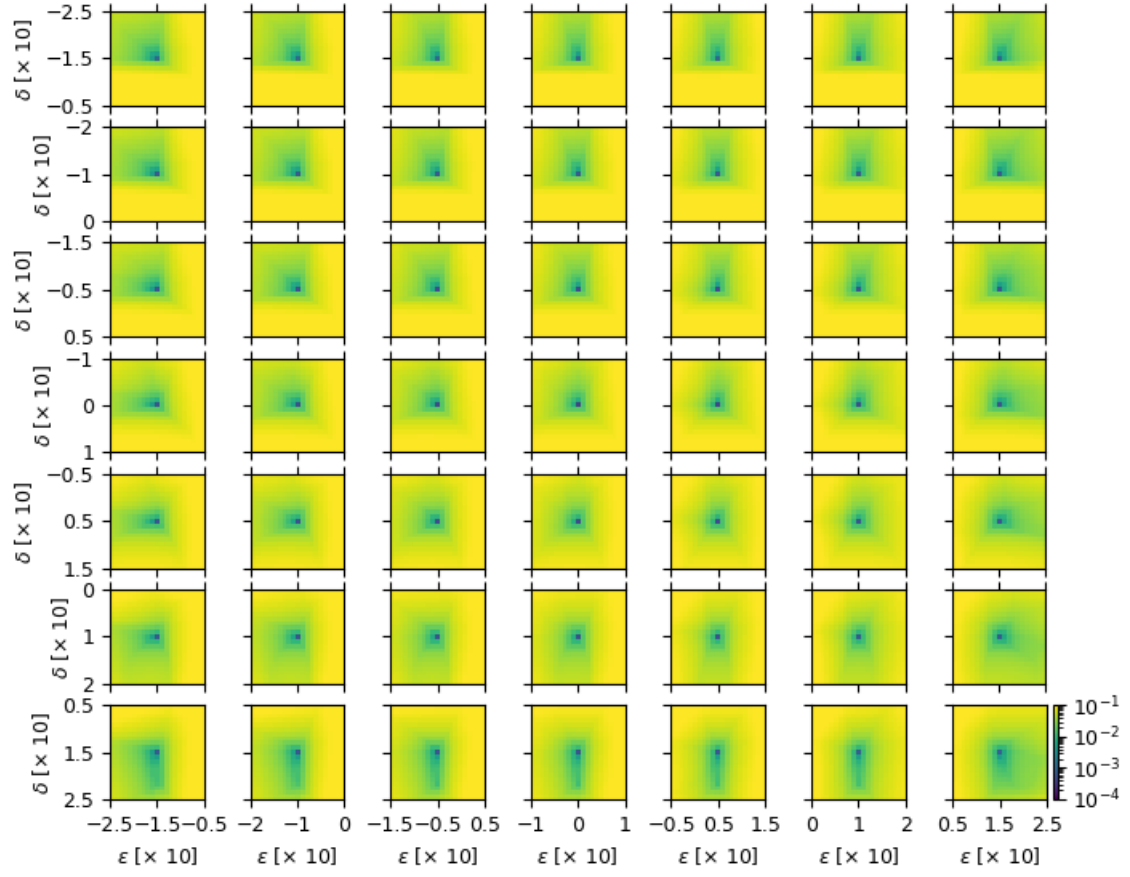


FIG. S5. 22 probe states. The figure is arranged as Fig. S2.

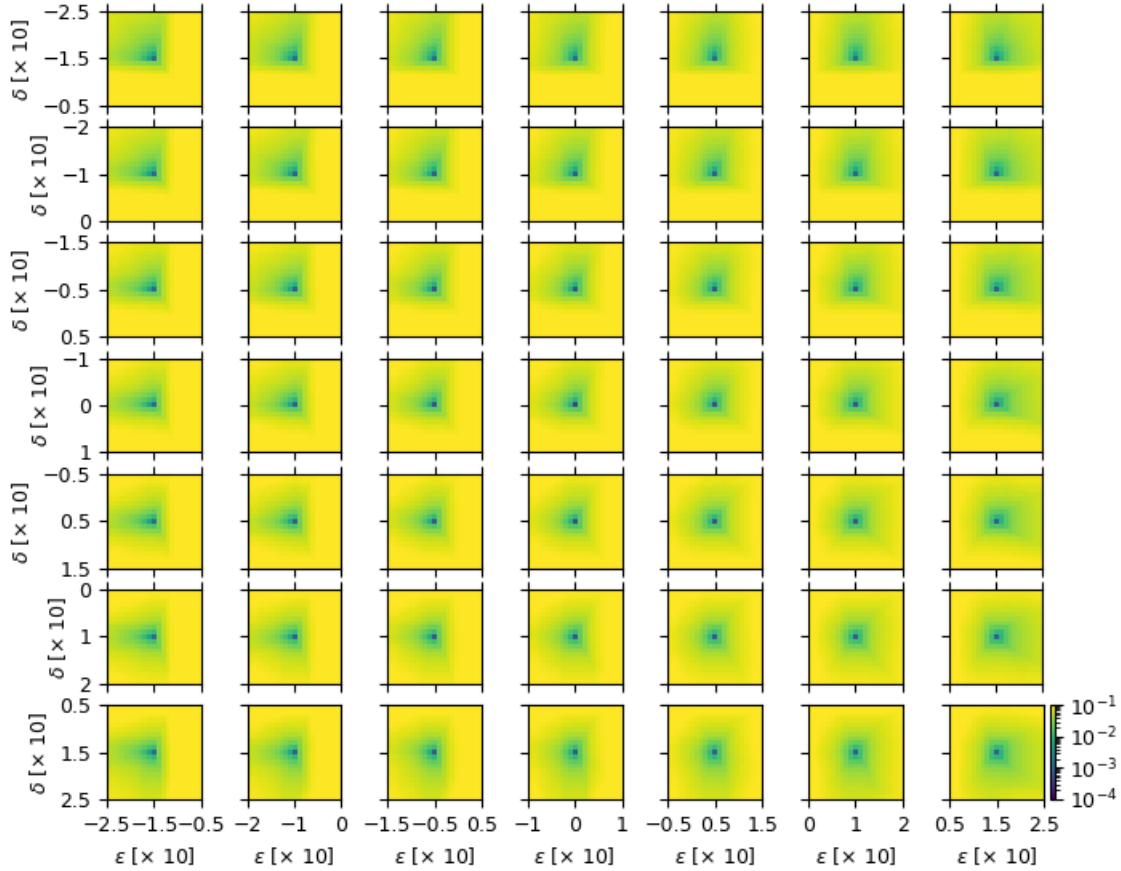


FIG. S6. 108 probe states. The figure is arranged as Fig. S2.

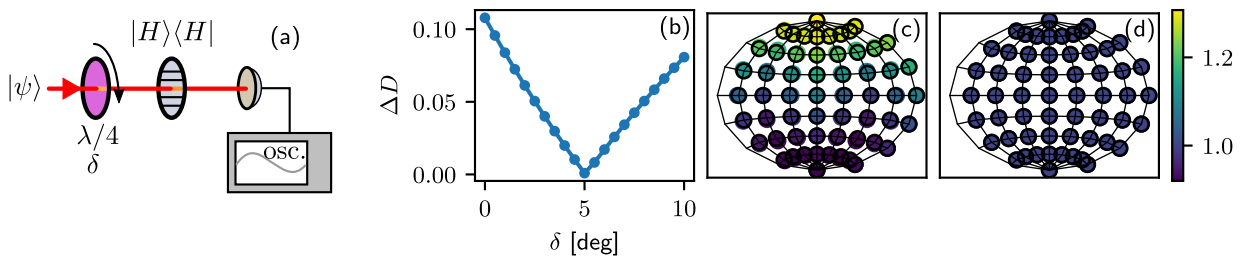


FIG. S7. Mitigation of artifact in rotating-waveplate polarimetry. (a) Measurement apparatus. A quarter-wave plate (purple) with retardance deviation $\delta' = 5$ deg is rotating in front of the linear polarizer. The photodiode signal is recorded and analyzed. (b) The minimal ΔD lies at the true retardance deviation δ' . (c) Initial mismatch results in state-dependent purity artifact. We plot the reconstructed probe states on the projected Bloch sphere and color-code their reconstructed stokes length $D = \sqrt{S_x^2 + S_y^2 + S_z^2}/S_0$. (d) When we considered the true retardance, the artifact vanished. Black circles depict the ideal testing states.